Coupling of light scattered by nanoparticles into waveguide modes in quantum-well solar cells

Daniel Derkacs[a], Winnie V. Chen[a], Peter Matheu[b], Swee H. Lim[a], Paul K. L. Yu[a], and E. T. Yu[a,*]
[a]Department of Electrical and Computer Engineering, University of California, San Diego
La Jolla, California 92093-0407
[b]Department of Electrical Engineering, University of California, Berkeley, Berkeley, CA 94720

ABSTRACT

We describe experimental and theoretical analysis of coupling of light scattered by metal or dielectric nanoparticles into waveguide modes of InP/InGaAsP quantum-well solar cells. The integration of metal or dielectric nanoparticles above the quantum-well solar cell device is shown to couple normally incident light into lateral optical propagation paths, with optical confinement provided by the refractive index contrast between the quantum-well layers and surrounding material. Photocurrent response spectra yield clear evidence of scattering of photons into the multiple-quantum-well waveguide structure, and consequently increased photocurrent generation, at wavelengths between the band gaps of the barrier and quantum-well layers. With minimal optimization, a short-circuit current density increase of 12.9% and 7.3% and power conversion efficiency increases of 17% and 1% are observed for silica and Au nanoparticles, respectively. A theoretical approach for calculating the optical coupling is described, and the resulting analysis suggests that extremely high coupling efficiency can be attained in appropriately designed structures.

Keywords: quantum-well solar cell, photovoltaics, nanoparticle, waveguide, plasmon, Mie scattering.

1. INTRODUCTION

There is currently great interest in the application of semiconductor nanostructures in photovoltaic devices including quantum-well structures,[1,2,3,4] nanowires,[5,6,7], and quantum dots.[8,9,10] Quantum-well solar cells and other 3rd generation cells have maximum theoretical power conversion efficiencies that range from 44.5%[3] to over 63%[11] and exceed the maximum theoretical single-junction limit of 31%.[12] However, the design and realization of quantum-well solar cell devices that have simultaneously high efficiency in both photon absorption and photogenerated carrier collection is highly challenging. Most notably, typical quantum-well solar cells suffer from a tradeoff between having of a sufficient number of quantum wells to ensure high photon absorption efficiency and the resulting reduction in photogenerated carrier collection efficiency. We show that the integration of metal or dielectric nanoparticles above the quantum-well solar cell device may be used to couple normally incident light into lateral optical propagation paths, with optical confinement provided by the refractive index contrast between the quantum-well layers and surrounding material. Substantially improved electrical current generation and collection over a broad range of wavelengths of incident light, and particularly at long wavelengths for which absorption occurs exclusively in the quantum-well layers, is observed. With optimization of optical mode structure and coupling, this approach is anticipated to enable large efficiency gains in quantum-well solar cells and other devices with thin active absorber regions.

2. DEVICE DESIGN

Lattice-matched InP/$In_{1-x}Ga_xAs_yP_{1-y}$ ($y \approx 2.2x$) multiple-quantum-well p-i-n solar cell structures, shown schematically in Fig. 1(a), were employed in our studies. Two sets of devices were studied. The n-type electrode of the p-i-n diode structure consisted of heavily doped InP, while the intrinsic region consisted of 10 nm $In_{0.91}Ga_{0.09}As_{0.2}P_{0.8}$ barriers

*) Electronic mail: ety@ece.ucsd.edu

Nanoscale Photonic and Cell Technologies for Photovoltaics, edited by Loucas Tsakalakos,
Proc. of SPIE Vol. 7047, 704703, (2008) · 0277-786X/08/$18 · doi: 10.1117/12.799666

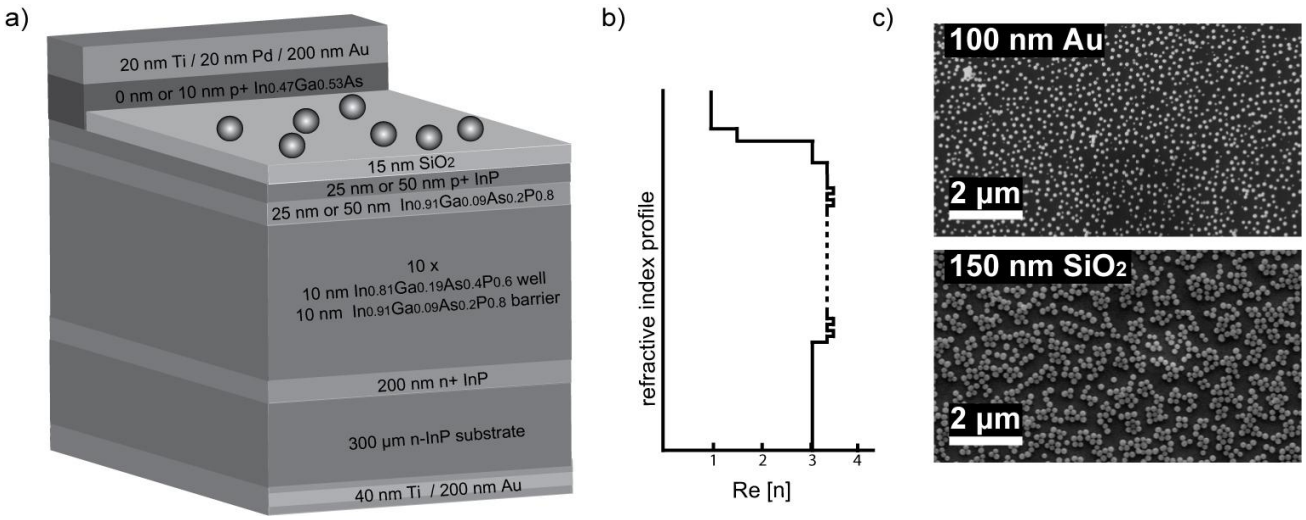

Fig. 1. (a) Schematic diagram of InP-based quantum-well solar cells with nanoparticles on the device surface. Device set A has a 250 nm thick intrinsic region consisting of quantum-wells, a 50 nm top barrier, and a 50 nm p-type InP contact layer. Device set B has a 225 nm thick intrinsic region consisting of quantum-wells, a 25 nm top barrier, a 25 nm p-type InP contact layer, and an additional 10 nm p-type InGaAs contact layer. (b) Refractive index profile of the quantum-well solar cell of part (a) with a 225 nm thick waveguide defined by the refractive index contrast between the quantum-well layers and surrounding material. (c) Scanning electron microscope images of 100 nm-diameter Au nanoparticles (top) and 150 nm-diameter SiO_2 nanoparticles (bottom) deposited on quantum-well solar cell device surface (device set B) at surface densities of 2.7×10^9 cm^{-2} and 2.1×10^9 cm^{-2} respectively.

alternating with 10 nm $In_{0.81}Ga_{0.19}As_{0.4}P_{0.6}$ quantum wells for ten periods with an additional 50 nm (device set A) or 25 nm (device set B) $In_{0.91}Ga_{0.09}As_{0.2}P_{0.8}$ barrier above the top quantum-well layer. The p-type electrode consisted of a heavily doped 50 nm p-type InP layer (set A) or 25 nm p-type InP plus 10 nm p-type $In_{0.47}Ga_{0.53}As$ (set B).

The key concept in a quantum-well solar cell device is that incorporation of a multiple-quantum-well layer within the intrinsic region of a p-i-n photovoltaic device enables its absorption spectrum to extend to longer wavelengths relative to that of a homojunction cell consisting entirely of the electrode material, yielding an increase in short-circuit current density (J_{sc}).[13] The resulting maximum power delivered for a quantum-well solar cell device can therefore exceed that of a corresponding homojunction device,[13,14] despite a drop in open-circuit voltage (V_{oc}) resulting from less-than-unity efficiency in collection of photogenerated carriers from the multiple-quantum-well layer. To optimize collection of photogenerated carriers from the quantum wells and to minimize the reduction of V_{oc}, a sufficiently large electric field across the intrinsic region – typically ~30 kV/cm or more[15,16] – must be maintained, and the barriers over which the carriers must be thermally or optically excited are typically 200-450 meV or less.[15,17,18,19] The former condition requires that the intrinsic region in the p-i-n diode be sufficiently thin, while the latter is satisfied by appropriate choice of quantum-well and barrier materials. For the device structure shown in
Fig. 1(a), with an intrinsic layer thickness of 250 nm, the electric field across the intrinsic region is estimated to be 48 kV/cm in equilibrium and 32 kV/cm at a maximum-power operating voltage of ~0.4 V, and the quantum well barriers are 44 meV and 66 meV for electrons and holes, respectively.

Intrinsic layer thicknesses sufficiently small to ensure efficient carrier collection are generally also small compared to the optical absorption length at wavelengths between the quantum-well and barrier/electrode absorption edges, resulting in poor efficiency in photon absorption at these wavelengths. However, incorporation of the multiple-quantum-well region, in addition to enabling photon absorption at longer wavelengths, also increases the refractive index within the intrinsic region relative to the surrounding electrode layers,[20,21] as shown in
Fig. 1(b), producing a slab waveguide structure. Scattering of incident light into lateral propagation paths that are optically confined by this waveguide can dramatically increase photon propagation lengths, and consequently photon

absorption efficiency. Indeed, waveguide mode coupling by light scattered from metallic nanoparticles has previously been demonstrated using metal nanoparticles on silicon-on-insulator (SOI) photodetectors.[22,23,24] Here, we achieve this scattering effect by deposition of metal or dielectric nanoparticles atop the semiconductor device, as shown in Fig. 1(c). Scattering of incident light by the nanoparticles then enables both improved transmission of photons into the semiconductor active layers and coupling of normally incident photons into lateral optically confined paths within the multiple-quantum-well waveguide layer, resulting in increased photon absorption, photocurrent, and power conversion efficiency.

3. EXPERIMENTAL METHODS

3.1 Quantum-well growth and characterization

All semiconductor epitaxial layers were grown in a horizontal quartz growth tube by metal organic chemical vapor deposition. For each sample, a 200 nm n-type InP buffer layer doped with Si at a concentration of ~8×10^{17} cm^{-3} was grown on an n-type (S doped, ~5×10^{18} cm^{-3}) InP substrate. For the quantum-well solar cell structures, a nominally undoped intrinsic multiple-quantum-well region was then grown that consisted of 10 nm $In_{0.91}Ga_{0.09}As_{0.2}P_{0.8}$ barriers and 10 nm $In_{0.81}Ga_{0.19}As_{0.4}P_{0.6}$ wells alternating for ten periods. A 50 nm (device set A) or 25 nm (device set B) nominally undoped $In_{0.91}Ga_{0.09}As_{0.2}P_{0.8}$ layer was then grown, followed by a 50 nm (set A) or 25 nm (set B) p-type InP layer (Zn doped, 3×10^{18} cm^{-3}) and a 10 nm p^+ $In_{0.47}Ga_{0.53}As$ cap layer (set B only) that facilitated Ohmic contact formation. For the barrier-only and InP homojunction control devices, the total nominally undoped intrinsic layer thicknesses were maintained at 250 nm (set A) or 225 nm (set B) but consisted entirely of $In_{0.91}Ga_{0.09}As_{0.2}P_{0.8}$ or InP, respectively, and the p-type and n-type epitaxial layers were unchanged. All layers were grown at a substrate temperature of 650°C except for the top Zn-doped p^+ layers which were grown at 525°C. Dopant concentrations and absorption edge wavelengths were measured on samples grown under conditions identical to those described above, and were determined by Hall measurements and room temperature photoluminescence, respectively. Epitaxial layer thicknesses and residual strain in the epitaxial layer structure were assessed by x-ray diffraction.

3.2 Contact formation

Large-area n-type Ohmic contacts were formed on the back of sample chips typically 1 cm^2 in area using 40 nm Ti/200 nm Au metallization deposited by electron-beam evaporation. 2 mm^2 active device window regions were defined by conventional photolithography, and p-type contacts were then formed using 20 nm Ti/20 nm Pd/200 nm Au metallization deposited by electron-beam evaporation and a standard lift-off process. No thermal annealing of the contacts was performed, in order to prevent Zn diffusion into the intrinsic region. The top $In_{0.47}Ga_{0.53}As$ contact layer (device set B only) was then removed from the window region by a selective wet etch (1:10:220 H_2SO_4:H_2O_2:H_2O for 15 sec), and a ~15 nm SiO_2 surface passivation layer was sputter deposited over the active window area of all devices.

3.3 Nanoparticle deposition and current-voltage measurement procedure

As preparation for nanoparticle deposition, all device structures were subjected to a 3 min exposure to a poly-L-lysine solution and blown dry with N_2. Current-voltage (*I-V*) characteristics were then measured using a Hewlett-Packard 4156a semiconductor parameter analyzer, both in the dark and under illumination provided by a Newport 96000 150 watt solar simulator with a xenon arc lamp under normal illumination incidence with no spectrum filter. Following the initial *I-V* measurements, devices were subjected to a 5-30 min exposure to a solution containing either 100 nm diameter Au or 150 nm diameter SiO_2 colloidal nanoparticles in a humid environment designed to minimize evaporation and consequent nanoparticle clustering, and then rinsed with de-ionized water and blown dry with N_2. These procedures yielded typical nanoparticle surface densities of ~$2\text{-}3\times10^9$ cm^{-2} as determined from scanning electron microscope images. *I-V* measurements were then performed on the resulting devices, both in the dark and under illumination. Current density, *J*, was computed by dividing the measured current by the device area as determined from optical microscope images of each device. A reference diode measured in parallel to the device under consideration was used to account for any fluctuations in the intensity of the illumination source over time, and device positioning and probing were sufficiently reproducible to yield measurement-to-measurement variation in electrical current within 1%.

3.4 Photocurrent measurement procedure

Photocurrent response spectra were measured using a 50 W tungsten halogen lamp as an illumination source and a monochromator with a 600 groove/mm grating, yielding monochromatic light for measurements extending over a wavelength range of 400–1200 nm. For measurements at wavelengths of 600-1000 nm, a red filter was employed to eliminate illumination from the second-order diffraction line; for measurements at wavelengths of 1000-1200 nm, a near-infrared filter was employed. Illumination was incident normal to the surface of the device under test through a chopper operating at 338 Hz, and the resulting photocurrent generated in the device was fed to a lock-in amplifier to isolate the signal component arising specifically from the incident illumination. A beam splitter was used to divert part of the light beam emerging from the monochromator to a Ge photodetector, the output of which was fed to a second lock-in amplifier. Spectral response curves as plotted in
Fig. 2 were calculated by dividing the directly measured response of a device by the measured Ge detector response and then multiplying the result by the known responsivity of the Ge detector.

4. RESULTS

4.1 Photocurrent response

Fig. 2(a) shows the spectral photocurrent response for InP homojunction, p-InP/i-$In_{0.91}Ga_{0.09}As_{0.2}P_{0.8}$/n-InP barrier-only, and p-i-n quantum-well solar cell devices from device set B. The epitaxial layer structures for these devices were grown by metal organic chemical vapor deposition in immediate succession under identical reactor conditions with identical i-layer thicknesses of 225 nm. The photocurrent response for the InP control sample extends only to the InP absorption edge at 960 nm, while for the barrier-only control and quantum-well devices the photocurrent responses extend to the absorption edges of $In_{0.91}Ga_{0.09}As_{0.2}P_{0.8}$ (1040 nm) and $In_{0.81}Ga_{0.19}As_{0.4}P_{0.6}$ (1160 nm), respectively. Fig. 2(b) shows the maximum-power curves for InP homojunction, p-InP/i-$In_{0.91}Ga_{0.09}As_{0.2}P_{0.8}$/n-InP barrier-only, and p-i-n quantum-well solar cell devices from device set A, grown in the same sequential manner as device set B, with i-layer thicknesses of

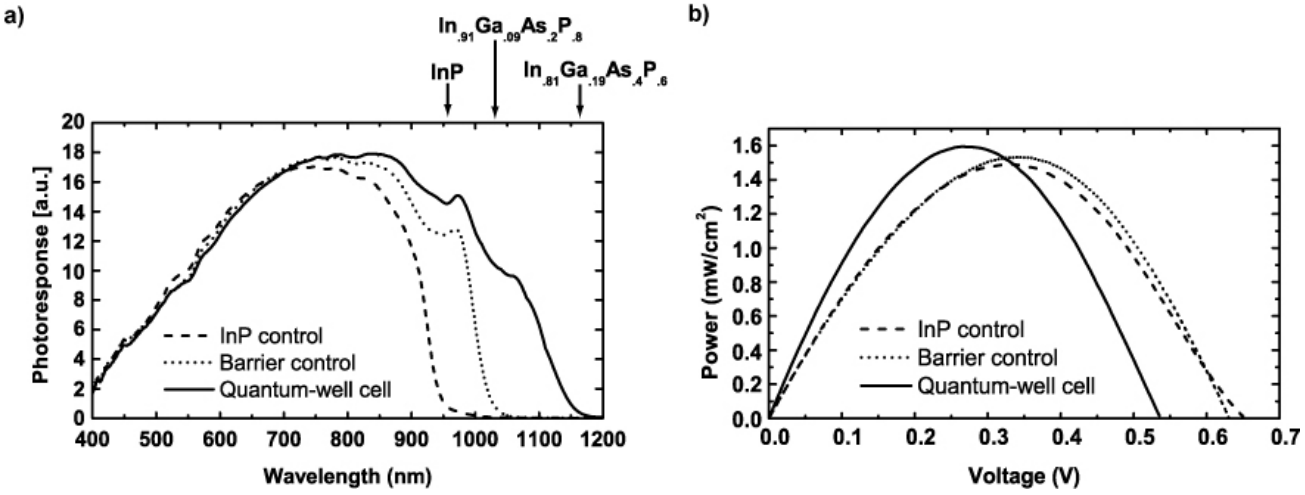

Fig. 2. (a) Photocurrent response spectra for the 225 nm thick i-layer device set B: InP *p-i-n* control device (dashed line), *p*-InP/*i*-$In_{0.91}Ga_{0.09}As_{0.2}P_{0.8}$/*n*-InP barrier-material control device (dotted line), and *p-i-n* 10-well $In_{0.91}Ga_{0.09}As_{0.2}P_{0.8}$/$In_{0.81}Ga_{0.19}As_{0.4}P_{0.6}$ quantum-well solar cell device (solid line) as shown in Fig. 1. The extended spectral response associated with incorporation of $In_{0.91}Ga_{0.09}As_{0.2}P_{0.8}$ and then of $In_{0.81}Ga_{0.19}As_{0.4}P_{0.6}$/$In_{0.91}Ga_{0.09}As_{0.2}P_{0.8}$ quantum wells is evident. The expected absorption edges of InP, $In_{0.91}Ga_{0.09}As_{0.2}P_{0.8}$, and $In_{0.81}Ga_{0.19}As_{0.4}P_{0.6}$ are indicated by the arrows. (b) Power output curves for device set A: Despite a drop in V_{oc}, the quantum-well device shows improved power conversion efficiency compared to the two control devices.

250 nm. Despite the drop in V_{oc} from 0.63-0.64 V for the homojunction and barrier-only devices to 0.53 V for the quantum-well devices, the quantum-well devices exhibit an increase in maximum power output of 7.4% and 4.6% relative to the homojunction and barrier-only devices, respectively. These results confirm that incorporation of lower-bandgap material indeed enables absorption of photons, and consequently generation of photocurrent, at wavelengths beyond the absorption edge of the InP electrode regions, and thereby improving power conversion efficiency.

To illustrate the effectiveness of nanoparticle scattering in improving photocurrent response and power conversion efficiency, we show in Fig. 3 photocurrent response spectra for quantum-well solar cells from device set B with either 100 nm diameter Au or 150 nm diameter SiO_2 nanoparticles deposited on the surface, plotted as ratios relative to the spectrum for the same device without nanoparticles. Surface particle densities of ~2.7×10^9 cm^{-2} and ~2.1×10^9 cm^{-2} were employed for Au and SiO_2 nanoparticles, respectively. Scattering of incident light by Au nanoparticles yields a reduction in photocurrent response at wavelengths of ~570 nm and below, and a broad increase from ~570 nm to >900 nm. This behavior arises from strong forward scattering of light by the nanoparticles combined with interference between the scattered wave and the waves directly transmitted across the semiconductor device surface. [25] For wavelengths above the surface plasmon polariton resonance wavelength at ~550nm, the phase of the Au nanoparticle polarizability, computed in the limit in which the particle radius is much smaller than the wavelength, is very small, ~0.1 radians or less. Thus, within the semiconductor, the electromagnetic wave arising from scattering by the nanoparticle is approximately in phase with that arising from direct transmission of the incident wave across the semiconductor-air interface, and these components will interfere constructively in the vicinity of the nanoparticle. For shorter wavelengths, however, the phase of the nanoparticle polarizability increases to a maximum of ~0.6 radians, resulting in a substantial phase shift, and partially destructive interference, between the electromagnetic field components arising from nanoparticle scattering and from direct transmission into the semiconductor. Scattering of incident light by SiO_2 nanoparticles yields an increased transmission and photocurrent response over the entire 400-1200 nm range of wavelengths as no surface plasmon polariton resonance is present.[26]

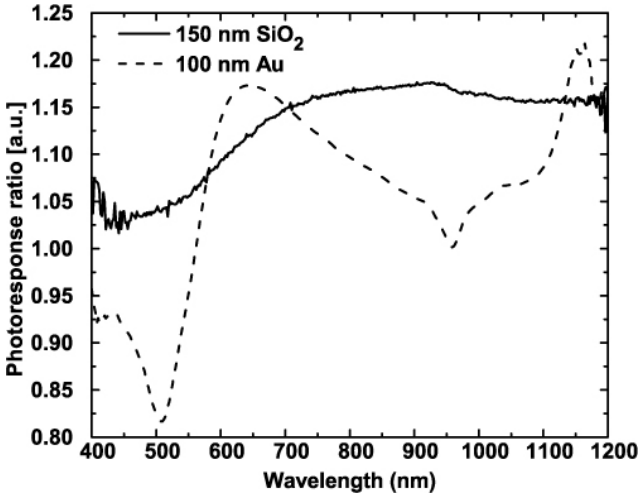

Fig. 3. Photocurrent response spectra of *p-i-n* $In_{0.91}Ga_{0.09}As_{0.2}P_{0.8}/In_{0.81}Ga_{0.19}As_{0.4}P_{0.6}$ quantum-well solar cells from device set B with either 100 nm diameter Au nanoparticles (dashed line) or 150 nm diameter SiO_2 nanoparticles (solid line) deposited on the surface, plotted as ratios relative to the spectrum for the same devices without nanoparticles. Surface densities of ~2.7×10^9 cm^{-2} and ~2.1×10^9 cm^{-2} were employed for Au and SiO_2 nanoparticles respectively.

For devices functionalized with Au nanoparticles we also observe a pronounced increase in photocurrent response between 960 nm and cutoff at ~1200 nm. We attribute this behavior to the scattering of incident radiation into optical propagation modes associated with the slab waveguide formed by the multiple-quantum-well region and surrounding layers. A standard calculation[27] shows that this waveguide supports two confined modes at wavelengths of 960-1200 nm. The improved photocurrent response in this wavelength range then arises because coupling of incident light into the guided and substrate radiation modes leads to a dramatic increase in photon path lengths within the multiple-quantum-well region associated with lateral, rather than vertical, photon propagation, and consequently greater efficiency in photon absorption.

4.2 Current-voltage characteristics

Previously, our group and others have reported increased J_{sc} and power conversion efficiency due to optical scattering from metal nanoparticles deposited on a-Si solar cells,[28] and Si solar cells.[25,29,30] The enhanced photocurrent response in nanoparticle-functionalized quantum-well solar cells observed here also leads to improved J_{sc} and power conversion efficiency under 150 watt white light illumination conditions. Fig. 4 shows current density-voltage characteristics and the corresponding power output for a quantum-well solar cell from device set B before and after deposition of SiO_2 nanoparticles on the device surface. For a SiO_2 nanoparticle surface density of ~2.1×10^9 cm^{-2}, a 12.9% increase in J_{sc}, an increase in the fill factor from 58% to 59%, and a 17.0% increase in maximum power conversion efficiency were observed relative to the same device prior to nanoparticle deposition. For an Au nanoparticle surface density of ~2.7×10^9 cm^{-2}, a 7.3% increase in J_{sc} and an increase of 1% in maximum power conversion efficiency relative to the same device prior to nanoparticle deposition were measured. Based on preliminary numerical simulations, substantially larger improvements are anticipated for devices with optimized nanoparticle sizes, size distributions, compositions, and densities, and employing epitaxial layer structures further optimized for coupling of incident radiation into lateral optical propagation paths. As we show in the following section, calculation of the coupling of radiation from a horizontal electric dipole located above the waveguide, representing light scattered by a nanoparticle, into these confined modes plus substrate radiation modes indicates that as much as 90% of the radiated (scattered) power can be coupled into these modes. Furthermore, with increasing wavelength the optical waveguide structure becomes better defined due to the wavelength dependence of the semiconductor refractive indices, resulting in increased coupling efficiency into the guided modes.[24]

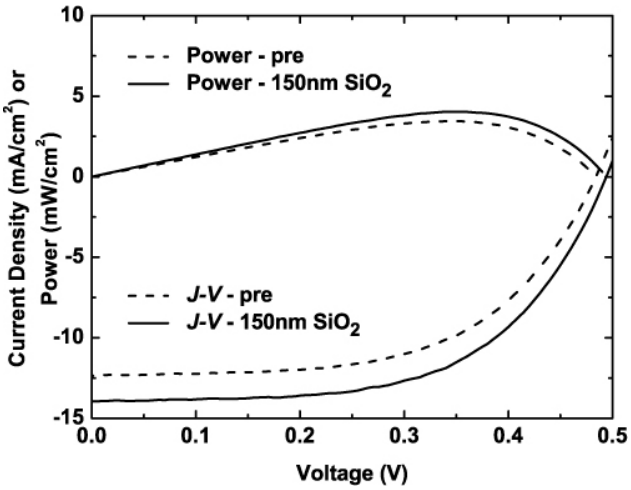

Fig. 4. *J-V* and output power curves measured for quantum-well solar cell devices (device set B) without SiO_2 nanoparticles (dashed lines), and for the same devices after deposition of 150 nm-diameter SiO_2 nanoparticles (solid lines). Short-circuit current density and maximum power increase by 12.9% and 17.0%, respectively, for devices incorporating SiO_2 nanoparticles.

5. WAVEGUIDE MODE COUPLING ANALYSIS

Light incident on metallic nanoparticles positioned above an underlying waveguide structure results in scattered dipolar fields that can couple into supported waveguide modes of the high refractive index guiding layers below, as depicted in Fig. 5(a). A model developed by Soller & Hall[31] shows that when a horizontal electric dipole is located above a silicon-on-insulator (SOI) substrate, up to 80%[23] of the light emitted by the dipole is coupled into the supported waveguide modes of the high refractive index guiding Si layer. In this model, based on classical radiation theory of an electric dipole oscillating in air above a plane-layered media, the dipole's total dissipated power, *P*, is calculated in terms of the vector field amplitudes of the modified dipole moment and local electric field due to the presence of the layered-media below. The vector field components can be expanded into an angular spectrum of plane waves by writing the fields as *k*-space integrals over the normalized wave-number *u,* where *u* is parallel to the z-axis and

$$u = \left[1 - k_x^2 / (\omega / c)^2\right]^{1/2} = \sin\theta . \quad (1)$$

Decomposing the field in this manner allows one to incorporate reflections in terms of the Fresnel reflection coefficients for transverse electric (TE) and transverse magnetic (TM) polarized light, r_s & r_p, respectively. The Fresnel reflection coefficients of our 26-layer air/SiO_2/multiple-quantum-well/substrate cell are then calculated by the transfer matrix method.[27] The resulting power spectrum for a horizontal electric dipole (HED) located directly above a plane-layered media is

$$S(u) = \int \frac{\partial P}{\partial u} du \propto \frac{u^3}{\left(1-u^2\right)^{1/2}} \left\{\left(1-u^2\right)\left[1-r_p\right] + \left[1+r_s\right]\right\}. \quad (2)$$

When $u \in (0,1)$, and subsequently $[\theta \in (0,\pi)]$, the full spectrum of propagating waves having nonzero $\pm\hat{x}$ wave vector components is represented. When $u \in (1,\infty)$, and subsequently $[\mathrm{Im}(\theta) \neq 0]$, the full spectrum of evanescent waves is represented. The waves emitted by the dipole can couple into three categories of modes as indicated in Fig. 5(b): waves that propagate above and below the air-cell interface $[u \in (0,1)]$, "leaky", or substrate radiation, modes that are evanescent above and propagating below the air-cell interface $[u \in (1, n_{InP})]$, and fully guided modes that are evanescent above and below the waveguide region within the cell $[u \in (n_{InP}, \infty)]$, where n_{InP} is the real part of the refractive index of the InP substrate.

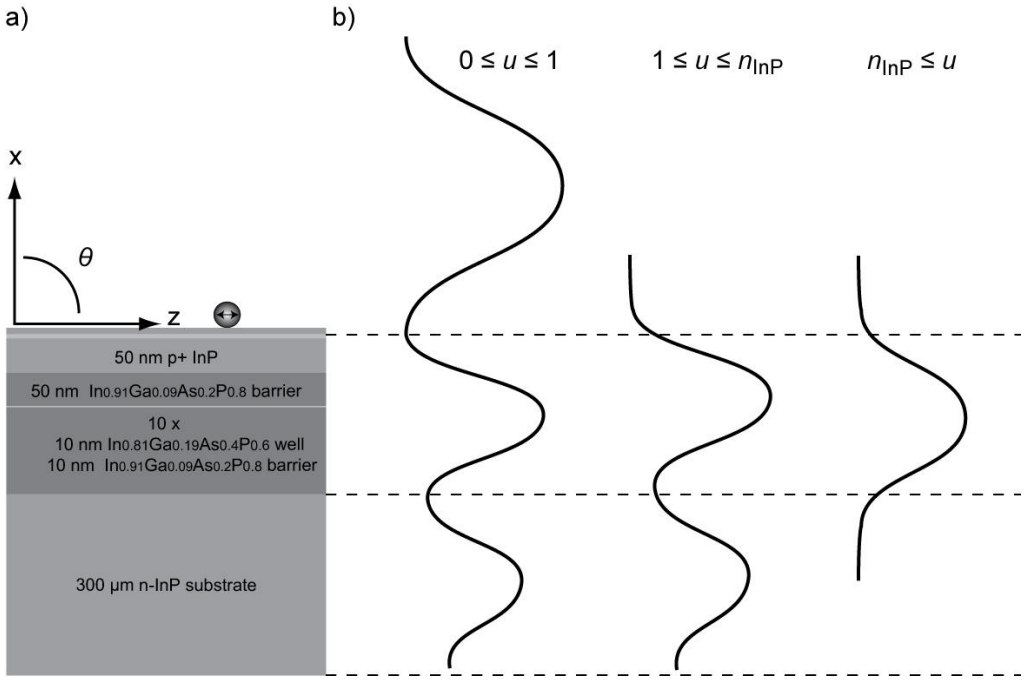

Fig. 5. (a) Schematic diagram of a horizontal electric dipole situated above a multiple-quantum-well solar cell structure. The darker shaded region is indicative of layers that have a higher index of refraction than the surrounding air or InP layers. (b) Representation of three categories of modes that waves emitted by the dipole can couple into. Waves that propagate above and below the air-cell interface occur when $u \in (0,1)$. So-called leaky waves occur when $u \in (1, n_{InP})$ and are evanescent above and propagating below the air-cell interface. Fully guided modes are evanescent above and below the waveguide region within the cell when $u \in (n_{InP}, \infty)$.

The power spectrum as a function of u for a horizontal electric dipole located above the multiple-quantum-well solar cell at various wavelengths is plotted in Fig. 6. The symbols near the top of the upper plot indicate the value of n_{InP} for each wavelength shown. The large peaks present in the plots for $u \geq n_{\mathrm{InP}}$ at each wavelength indicate strong coupling into the guided optical modes of the multiple-quantum well waveguide region. The greatest coupling occurs at 1150 nm as

indicated by the sharp peaks at u = 3.246 (TM0 mode) and u = 3.252 (TE0 mode). As the wavelength decreases, the modal peaks merge together due to increasing absorption in the material. It is clear that there is a strong behavioral correlation in coupled power spectrum and the photocurrent response ratio for Au nanoparticles shown in Fig. 3.

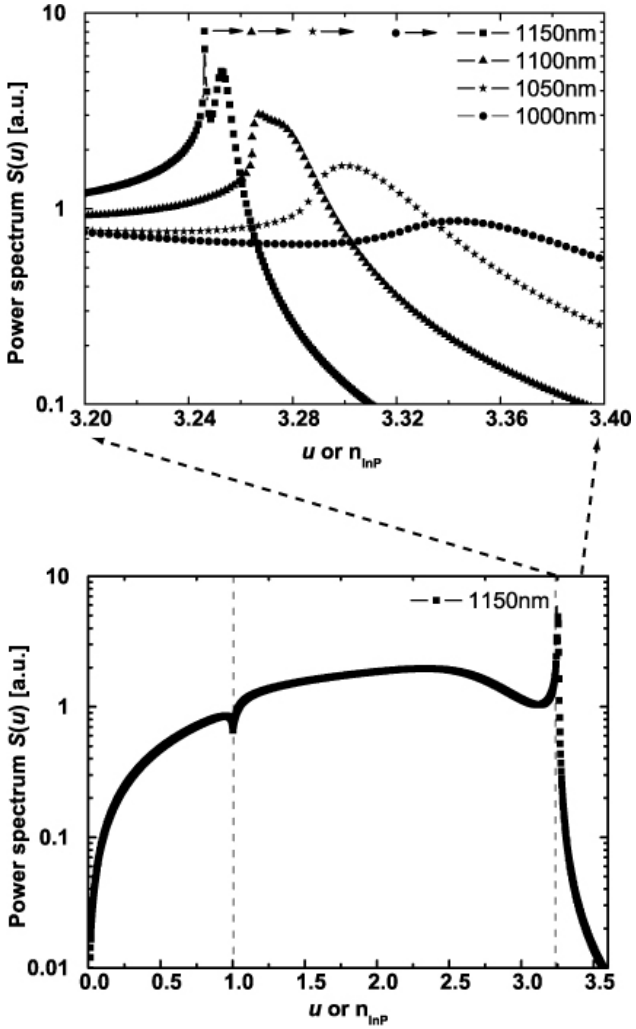

Fig. 6. Calculated power spectrum, S(u), for a horizontal electric dipole located above a multiple-quantum-well solar cell. In the lower plot, the vertical dashed lines delineate the three regions that light can couple into: (from left to right) propagating, leaky, and guided. The magnified view in the upper plot shows S(u) for wavelengths ranging from 1000nm to 1150nm. The symbols near the top of the upper plot indicate the value of nInP and consequently the onset of guided mode coupling (for u>nInP) at 1150 nm (squares), 1100 nm (triangles), 1050 nm (stars), and 1000 nm (circles). The peaks present in the plots for u ≥ nInP indicate strong coupling into the guided optical modes of the multiple-quantum well waveguide region. The greatest coupling occurs at 1150 nm as indicated by the sharp peak on the left (TM0 mode) and on the right (TE0 mode). As the wavelength decreases, the modal peaks merge together due to increasing absorption in the material. Note the strong correlation in coupled power spectrum and the photocurrent response ratio for Au nanoparticles shown in Fig. 3.

The ratio of the power radiated into a fully guided mode to the total radiated power, given by

$$\int_{n_{InP}}^{\infty} S(u)du \Big/ \int_{0}^{\infty} S(u)du\,, \tag{3}$$

was computed for wavelengths ~600-1200 nm and it was found that coupling of radiation from a HED into the slab waveguide modes occurs with an efficiency <10%. However, coupling of radiation from a HED into either a guided or a substrate radiation modes, given by

$$\int_1^\infty S(u)du \Big/ \int_0^\infty S(u)du\,, \tag{4}$$

occurs with an efficiency of 88-92% over the ~600-1200nm wavelength range. This result suggests that with optimization of optical mode structure and coupling, of material absorption properties, and of electric field profiles for carrier collection efficiency, a large increase in power conversion efficiency due to absorption of long-wavelength photons in the quantum wells within the waveguiding region should be attainable.

6. CONCLUSION

In summary, we have shown that the performance of quantum-well solar cells can be substantially improved by integration of dielectric or metal nanoparticles with the semiconductor device to couple normally incident light into lateral propagation paths confined within the slab waveguide formed by the multiple-quantum-well intrinsic layer. This approach enables the conflict normally inherent in achieving both efficient photon absorption (mandating a thick multiple-quantum-well layer) and efficient collection of photogenerated carriers (typically requiring a thin multiple-quantum-well layer) to be circumvented, and could help enable realization of the very high maximum power conversion efficiencies predicted for quantum-well solar cells. Furthermore, the concepts demonstrated here are expected to be broadly applicable to a variety of other advanced photovoltaic structures, such as intermediate-band solar cells and various other thin-film devices, as well as other types of semiconductor-based photodetectors in which wavelength-specific enhancement of photoresponse is desired.

ACKNOWLEDGEMENTS

Part of this work was supported by a grant from the UCSD Von Liebig Foundation, by AFOSR (FA9550-07-1-0148), and by DoE (DE-FG36-08GO18016). Correspondence should be addressed to E.T.Y.

REFERENCES

[1] Barnham, K. W. J., Ballard, I., Connolly, J. P., Ekins-Daukes, N. J., Kluftinger, B. G., Nelson, J., and Rohr, C., "Quantum well solar cells," Physica E 14(1), 27-36 (2002).

[2] Johnson, D. C., Ballard, I. M., Barnham, K. W. J., Connolly, J. P., Mazzer, M., Bessière, A. Calder, C., Hill, G., and Roberts, J. S., "Observation of photon recycling in strain-balanced quantum well solar cells," Appl. Phys. Lett. 90(21), 213505 (2007).

[3] Wei, G., Shiu, K. T., Giebink, N. C., and Forrest, S. R., "Thermodynamic limits of quantum photovoltaic cell efficiency," Appl. Phys. Lett. 91(22), 223507 (2007).

[4] Anderson, N. G., "On quantum well solar cell efficiencies," Physica E 14(1), 126-131 (2002).

[5] Xiangfeng, D., Huang, Y., Cui, Y., Wang, J., and Lieber, C. M., "Indium phosphide nanowires as building blocks for nanoscale electronic and optoelectronic devices," Nature 409, 66-69 (2001).

[6] Law, M., Greene, L. E., Johnson, J. C., Saykally, R., and Yang, P., "Nanowire dye-sensitized solar cells," Nat. Mater. 4, 455-459 (2005).

[7] Tsakalakos, L., Balch, J., Fronheiser, J., Korevaar, B. A., Sulima, O., and Rand, J., "Silicon nanowire solar cells," Appl. Phys. Lett. 91(23), 233117 (2007).

[8] Barnham, K.W.J., Marques, J.L., Hassard, J., and O'Brien, P., "Quantum-dot concentrator and thermodynamic model for the global red shift," Appl. Phys. Lett. 76(9), 1197-1199 (2000).

[9] McDonald, S. A., Konstantatos, G., Zhang, S., Cyr, P. W., Klem, E. J. D., Levina, L., and Sargent, E. H., "Solution-processed PbS quantum dot infrared photodetectors and photovoltaics," Nat. Mater. 4, 138-142 (2005).

[10] Klimov, V. I., "Detailed-balance power conversion limits of nanocrystal-quantum-dot solar cells in the presence of carrier multiplication," Appl. Phys. Lett. 89(12), 123118 (2006).

[11] Bremner, S. P., Corkish, R., and Honsberg, C.B., "Detailed balance efficiency limits with quasi-Fermi level variations," IEEE Trans. Electron. Devices 46(10), 1932-1939 (1999).

[12] Henry, C. H., "Limiting efficiencies of single and multiple energy gap terrestrial solar cells," J. Appl. Phys. 51(8), 4494-4500 (1980).

[13] Barnham, K. W. J., Braun, B., Nelson, J., Paxman, M., Button, C., Roberts, and J. S., Foxon, C. T., "Short-circuit current and energy efficiency enhancement in a low-dimensional structure photovoltaic device," Appl. Phys. Lett. 59(1), 135-137 (1991).

[14] Raisky, O. Y., Wang, W. B., Alfano, R. R., Reynolds, C. L. Jr., Stampone, D. V., and Focht, M. W., "$In_{1-x}Ga_xAs_{1-y}P_y$/InP multiple quantum well solar cell structures," J. Appl. Phys. 84(10), 5790-5794 (1998).

[15] Alemu, A., Coaquira, J. A. H., and Freundlich, A., "Dependence of device performance on carrier escape sequence in multi-quantum-well p-i-n solar cells," J. Appl. Phys. 99(8), 084506 (2006).

[16] Serdiukova, I., Monier, C., Vilela, M. F., and Freundlich, A., "Critical built-in electric field for an optimum carrier collection in mulitquantum well p-i-n diodes," Appl. Phys. Lett 74(19), 2818-2814 (1999).

[17] Anderson, N. G., "Ideal theory of quantum well solar cells," J. Appl. Phys. 78(3), 1850-1861 (1995).

[18] Mohaidat, J. M., Shum, K., Wang, W. B., Alfano, R. R., "Barrier potential design criteria in multiple-quantum-well-based solar-cell structures," J. Appl. Phys. 76(9), 5533–5537 (1994).

[19] Ramey, S. M., Khoie, R., "Modeling of multiple-quantum well solar cells including capture, escape, and recombination of photoexcited carriers in quantum wells," IEEE Trans. Electron Devices 50(5), 1179-1188 (2003).

[20] Adachi, S., "Optical dispersion relations for GaP, GaAs, GaSb, InP, InAs, InSb, $Al_xGa_{1-x}As$, and $In_{1-x}Ga_xAs_yP_{1-y}$," J. Appl. Phys. 66(12), 6030-6040 (1989).

[21] Jensen, B., and Torabi, A., "Refractive index of quaternary $In_{1-x}Ga_xAs_yP_{1-y}$ lattice matched to InP," J. Appl. Phys. 54(6), 3623-3625 (1983).

[22] Stuart, H. R., and Hall, D. G., "Island size effects in nanoparticle-enhanced photodetectors," Appl. Phys. Lett. 73(26), 3815-3817 (1998).

[23] Soller, B. J., Stuart, H. R., and Hall, D. G., "Energy transfer at optical frequencies to silicon-on-insulator structures," Optics Lett. 26(18), 1421-1423 (2001).

[24] Catchpole, K. R., and Pillai, S., "Absorption enhancement due to scattering by dipoles into silicon waveguides," J. Appl. Phys. 100(4), 044504 (2006).

[25] Lim, S. H., Mar, W., Matheu, P., Derkacs, D., and Yu, E. T., "Photocurrent spectroscopy of optical absorption enhancement in silicon photodiodes via scattering from surface plasmon polaritons in gold nanoparticles," J. Appl. Phys. 101(10), 104309 (2007).

[26] Sundararajan, S. P., Grady, N. K., Mirin, N., and Halas, N. J., "Nanoparticle-Induced Enhancement and Suppression of Photocurrent in a Silicon Photodiode," Nano Lett. 8(2), 624-630 (2008).

[27]P. Yeh, [Optical Waves in Layered Media], John Wiley & Sons, New York, 319 (1988).

[28] Derkacs, D., Lim, S. H., Matheu, P., Mar, W., and Yu, E. T. "Improved performance of amorphous silicon solar cells via scattering from surface plasmon polaritons in nearby metallic nanoparticles," J. Appl. Phys. 89(9), 093103 (2006).

[29] Schaadt, D. M., Feng, B., and Yu, E. T., "Enhanced semiconductor optical absorption via surface plasmon excitation in metal nanoparticles," Appl. Phys. Lett. 86(6), 063106 (2005).

[30] Pillai, S., Catchpole, K. R., Trupke, T., and Green, M. A., "Surface plasmon enhanced silicon solar cells," J. Appl. Phys. 101(9), 093105 (2007).

[31] Soller, B. J., Stuart, H. R., and Hall, D. G., "Energy transfer at optical frequencies to silicon based waveguiding structures,". J. Opt. Soc. Am. A 18(10), 2577-2584 (2001).